DOI: 10.1021/ic100028y

Inorganic Chemistry
Article

Ligand-Centered Redox Activity: Redox Properties of 3d Transition Metal Ions Ligated by the Weak-Field Tris(pyrrolyl)ethane Trianion

Graham T. Sazama and Theodore A. Betley*

Department of Chemistry and Chemical Biology, Harvard University, 12 Oxford Street, 306E Mallinckrodt, Cambridge, Massachusetts 02138

Received January 5, 2010

First-row transition metal complexes of the tris(pyrrolyl)ethane (tpe) trianion have been prepared. The tpe ligand was found to coordinate in a uniform η^1,η^1,η^1-coordination mode to the divalent metal series as revealed by X-ray diffraction studies. Magnetic and structural characterization for complexes of the type $[(tpe)M^{II}(py)][Li(THF)_4]$ (M: Mn, Fe, Co, Ni) reveal each divalent ion to be high-spin and have a distorted trigonal-monopyramidal geometry in the solid state. The pyridine ligand binds significantly canted from the molecular C_3 axis due to a stabilizing π-stacking interaction with a ligand mesityl substituent. Cyclic voltammetry on the $[(tpe)M^{II}(py)]^-$ series reveals a common irreversible oxidation pathway that is entirely ligand-based, invariant to the divalent metal bound. This latter observation indicates that fully populated ligand-based orbitals from the tpe construct are energetically most accessible in the electrochemical experiments, akin to their dipyrromethane analogues. Chemical oxidation of $[(tpe)Fe^{II}(py)]^-$ yields a product in which the ligand has dissociated one pyrrole (following tpe oxidation and H-atom abstraction) and binds a second equivalent of pyridine to form the neutral, tetrahedral Fe^{II} species (κ^2-tpe)$Fe(py)_2$. Similarly, chemical oxidation of the Zn(II) analogue shows evidence for tpe oxidation by electron paramagnetic resonance spectroscopy (77 K, toluene glass) with an isotropic signal for the organic radical at $g = 2.002$. Density functional theory analysis on this family of complexes reveals that the highest lying molecular orbitals are completely ligand-based, corroborating our proposed electronic structure assignment.

I. Introduction

Cooperative molecular redox comprised of metal and ligand contributions requires both energetic and angular overlap between the frontier ligand-based π orbitals and the metal-based d orbitals.[1] Pyrrole-based, oligomeric ligand platforms are an important subclass of the prototypical redox-active ligand platforms. Porphyrin[2] π electrons in metal porphyrin complexes are typically inert with the exception of compound I in cytochrome P450, wherein a single oxidizing equivalent is stored in the porphyrin macrocyle.[3] In the case of porphyrinogen systems,[4] the pyrrole subunits are unconjugated and thus have higher energy π orbitals, which results in increased ligand participation in molecular redox events. Transition metal complexes of both

*To whom correspondence should be addressed. E-mail: betley@chemistry.harvard.edu.

(1) Common redox active ligands: *Catecholates* :(a) Haga, M.; Dodsworth, E. S.; Lever, A. B. P. *Inorg. Chem.* **1986**, *25*, 447–453. (b) Masui, H.; Lever, A. B. P.; Auburn, P. R. *Inorg. Chem.* **1991**, *30*, 2402−2410. Dithiolates: (c) Schrauzer, G. N.; Mayweg, V. *J. Am. Chem. Soc.* **1962**, *84*, 3221. (d) Stiefel, E. I.; Waters, J. H.; Billig, E.; Gray, H. B. *J. Am. Chem. Soc.* **1965**, *87*, 3016−3017. Amido-phenolates:(e) Chaudhuri, P.; Verani, C. N.; Bill, E.; Bothe, E.; Weyhermüller, T.; Wieghardt, K. *J. Am. Chem. Soc.* **2001**, *123*, 2213–2223. (f) Herebian, D.; Bothe, E.; Bill, E.; Weyhermüller, T.; Wieghardt, K. *J. Am. Chem. Soc.* **2001**, *123*, 10012–10023. (g) Blackmore, K. J.; Ziller, J. W.; Heyduk, A. F. *Inorg. Chem.* **2005**, *44*, 5559–5561. (h) Haneline, M. R.; Heyduk, A. F. *J. Am. Chem. Soc.* **2006**, *128*, 8410–8411. (i) Blackmore, K. J.; Lal, N.; Ziller, J. W.; Heyduk, A. F. *J. Am. Chem. Soc.* **2008**, *130*, 2728−2730. Phenolates:(j) Hockertz, J.; Steenken, S.; Wieghardt, K.; Hildebrandt, P. *J. Am. Chem. Soc.* **1993**, *115*, 11222–11230. (k) Chaudhuri, P.; Hess, M.; Muller, J.; Hildenbrand, K.; Bill, E.; Weyhermüller, T.; Wieghardt, K. *J. Am. Chem. Soc.* **1999**, *121*, 9599−9610. Imino-pyridines:(l) Bouwkamp, M. W.; Bowman, A. C.; Lobkovsky, E.; Chirik, P. J. *J. Am. Chem. Soc.* **2006**, *128*, 13340–13341. (m) Bart, S. C.; Chlopek, K.; Bill, E.; Bouwkamp, M. W.; Lobkovsky, E.; Neese, F.; Wieghardt, K. *J. Am. Chem. Soc.* **2006**, *128*, 13901–13912. (n) Bart, S. C.; Lobkovsky, E.; Bill, E.; Wieghardt, K.; Chirik, P. J. *Inorg. Chem.* **2007**, *46*, 7055–7063.

(2) Kadish, K. M.; Smith, K. M.; Guilard, R. *The Porphyrin Handbook*; Academic Press: San Diego, CA, 2003; Vols. *15*−*20*.

(3) (a) Watanabe, Y. In *The Porphyrin Handbook*; Kadish, K. M., Smith, K. M., Guilard, R., Eds.; Academic Press: New York, 2000; Vol. *4*, pp 97−118. (b) Schulz, C. E.; Devaney, P. W.; Winkler, H.; Debrunner, P. G.; Doan, N.; Chiang, R.; Rutter, R.; Hager, L. P. *FEBS Lett.* **1979**, *103*, 102–105. (c) Groves, J. T.; Haushalter, R. C.; Nakamura, M.; Nemo, T. E.; Evans, B. J. *J. Am. Chem. Soc.* **1981**, *103*, 2884–2886. (d) Penner-Hahn, J. E.; Smith Eble, K.; McMurry, T. J.; Renner, M.; Balch, A. L.; Groves, J. T.; Dawson, J. H.; Hodgson, K. O. *J. Am. Chem. Soc.* **1986**, *108*, 7819–7825.

(4) (a) Floriani, C.; Floriani-Moro, R. In *The Porphyrin Handbook*; Academic Press: San Diego, CA, 2003; Vol. *3*, pp 405−420. (b) Jubb, J.; Floriani, C.; Chiesi-Villa, A.; Rizzoli, C. *J. Am. Chem. Soc.* **1992**, *114*, 6571–6573. (c) Piarulli, U.; Solari, E.; Floriani, C.; Chiesi-Villa, A.; Rizzoli, C. *J. Am. Chem. Soc.* **1996**, *118*, 3634–3642. (d) Crescenzi, R.; Solari, E.; Floriani, C.; Chiesi-Villa; Rizzoli, C. *J. Am. Chem. Soc.* **1999**, *121*, 1695–1706. (e) Bachmann, J.; Nocera, D. G. *J. Am. Chem. Soc.* **2004**, *126*, 2829–2837. (f) Bachmann, J.; Nocera, D. G. *J. Am. Chem. Soc.* **2005**, *127*, 4730–4733.

Published on Web 01/26/2010

Scheme 1

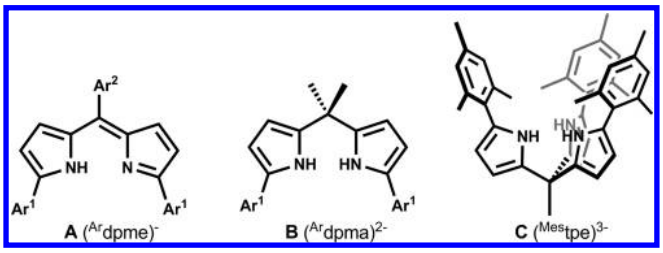

of these tetra-pyrrole macrocycle systems feature transition metal and ligand π-orbital alignment such that coupling of the two reservoirs is permitted.

Our recent interest in pyrrole-based ligands stems from our desire to determine if the rich redox chemistry which features prominently in metal−porphyrin and porphyrinogen complexes would translate to more easily synthesized truncated frameworks (Scheme 1). Dipyrromethenes (A, Scheme 1),[5] like their porphyrin analogs, exhibit reversible, ligand-based redox events which are almost entirely decoupled from metal-based redox activity.[6] Dipyrromethane complexes (B, Scheme 1),[7] in contrast, display surprisingly uniform electrochemical behavior despite differences in metal valence electron configuration, geometry, and spin state.[8] The energetically high-lying π electrons from the dipyrromethane framework almost exclusively account for the observed redox behavior of the metal complexes studied, indicating that fully populated ligand-based orbitals from the dipyrromethane construct lie above partially filled metal 3d orbitals. Whereas the macrocylic nature of porphyrinogens stabilizes ligand-centered radicals through the reversible formation of C−C bonds within the macrocycle,[4] the dipyrromethane metal complexes do not exhibit similar reactivity. Chemical oxidation of the metal−dipyrromethane complexes does not yield stable ligand-based diradical/dicationic species or readily identified metal-containing products. Thus, we sought to develop a similar pyrrole-derived ligand platform that would be more amenable to the study of the resulting oxidation products.

Sterically encumbered, trianionic tris(pyrrolyl)ethane ligands (C, Scheme 1)[9] are potential candidates to circumvent the instability of the dipyrromethane analogues while maintaining the attractive attributes of these platforms (e.g., redox activity, attenuated N π donicity). We hypothesized that a tris(pyrrolyl)ethane triply deprotonated and bound κ^3 to a divalent metal ion should be easier to oxidize than their neutral dipyrromethane analogues and may confer greater stability to the oxidized products.[10] Furthermore, the tris-(pyrrolyl)ethane platform, along with the dipyrromethene and dipyrromethane systems, relaxes the structural rigidity porphyrins and porphyrinogens require, opening the coordination sphere of the bound transition metal considerably.

II. Results

II.a. Synthesis and Characterization of [tpe] and Its Metal Complexes. The synthesis of the tris(pyrrolyl)ethane ligand was accomplished using a modified acid-catalyzed[9a] condensation reaction between 2-mesityl pyrrole, 1.5 equiv of trimethylorthoformate, and ∼7% loading of pyridinium *p*-toluenesulfonate acid catalyst in two portions.[6,8] Refluxing this mixture in dichloromethane for several days, followed by flash chromatography and trituration with hexanes, cleanly affords 1,1,1-tris(2-mesitylpyrrolyl)ethane ($tpeH_3$, **1**) as a pale yellow-white solid in greater than 69% isolated yield (Scheme 2). To assess the steric and electronic properties that **1** imparts, transition metal complexes of the tpe ligand were prepared in the following manner: reaction of **1** with 3.1 equiv of phenyllithium ($LiN(SiMe_3)_2$ works equally well) in tetrahydrofuran generates the trilithio complex ($tpeLi_3$), which can be isolated but was typically prepared in situ for the following syntheses. The in situ generated trilithio species was then reacted with a stoichiometric amount of a divalent metal precursor (i.e., $MCl_2(py)_2$; M = Mn, Co, Fe, Ni, Zn; py = pyridine) in thawing THF solutions to afford the metalated salts of the type $[(tpe)M(py)][Li(THF)_4]$ upon isolation via crystallization (M = pale yellow Mn (**2**), bright orange Fe (**3**), blue Co (**4**), green Ni (**5**), and yellow-orange Zn (**6**)). The tpe ligand was found to uniformly bind in an η^1,η^1,η^1-coordination mode, strictly enforcing a four-coordinate geometry at the metal ion, as confirmed by X-ray diffraction studies (Table 1). The solid state molecular structures for the tetrahedral Mn (**2**), Fe (**3**), Co (**4**), Ni (**5**), and Zn (**6**) complexes are shown in Figure 1.

II.b. Structural Characterization of Complexes 2−6. Complexes **2**−**6** are nearly isostructural, featuring an intermediate geometry between trigonal-monopyramidal and pseudotetrahedral at the metal center. The pyridine ligand and two of the tpe pyrrolide substituents (N_b, N_c) form the trigonal base with one pyrrolide ligand (N_a) capping the trigonal monopyramid. The sum of the angles of the monopyramidal base (N_{py}, N_b, N_c) $\alpha+\beta+\varphi_{bc}$ sum to nearly 360° for each complex ($\alpha+\beta+\varphi_{bc}$ (deg): M_n 347, Fe 350, Co 348, Ni 351, Zn 348). The pyridine ligand is consistently positioned off the molecular 3-fold axis (axis depicted **d** in the diagram for Table 2), positioning the pyridine ligand in a distinct π-stacking interaction with the N_a pyrrolide mesityl substituent (ranging from 3.5 to 4.0 Å separation between the pyridine centroid and the mesityl centroid).[11] The angle θ describes the orientation of the pyridine ligand with the (tpe)M fragment C_3 axis, such that a θ of 180° would describe a perfect C_3

(5) Wood, T. E.; Thompson, A. *Chem. Rev.* **2007**, *107*, 1831–1861.
(6) King, E. R.; Betley, T. A. *Inorg. Chem.* **2009**, *48*, 2361–2363.
(7) (a) Lee, C.-H.; Lindsey, J. S. *Tetrahedron* **1994**, *50*, 11427–11440. (b) Jones, D. J.; Gibson, V. C. *Heterocycles* **2006**, *68*, 1121–1127. (c) Swartz, D. L.; Odom, A. L. *Organometallics* **2006**, *25*, 6125–6133. (d) Novak, A.; Blake, A. J.; Wilson, C.; Love, J. B. *Chem. Commun.* **2002**, 2796–2797. (e) Love, J. B.; Salyer, P. A.; Bailey, A. S.; Wilson, C.; Blake, A. J.; Davies, E. S.; Evans, D. J. *Chem. Commun.* **2003**, 1390–1391.
(8) King, E. R.; Betley, T. A. *J. Am. Chem. Soc.* **2009**, *131*, 14374–14380.
(9) (a) Wang, Q. M.; Bruce, D. W. *Synlett* **1995**, 1267–1268. (b) Barnard, T. S.; Mason, M. R. *Inorg. Chem.* **2001**, *40*, 5001–5009. (c) Reese, C. B.; Yan, H. *Tetrahedron Lett.* **2001**, *42*, 5545–5547. (d) Beer, P. D.; Cheetham, A. G.; Drew, M. G. B.; Fox, O. D.; Hayes, E. J.; Rolls, T. D. *Dalton Trans.* **2003**, *4*, 603–611. (e) Betley, T. A.; Surendranath, Y.; Childress, M. V.; Alliger, G. E.; Fu, R.; Cummins, C. C.; Nocera, D. G. *Philos. Trans. Royal Soc. B* **2008**, *363*, 1293–1303.
(10) (a) Byrne, E. K.; Theopold, K. H. *J. Am. Chem. Soc.* **1987**, *109*, 1282–1283. (b) Barner, C. J.; Collins, T. J.; Mapes, B. E.; Santarsiero, B. D. *Inorg. Chem.* **1986**, *25*, 4322–4323. (c) Collins, T. J.; Kostka, K. L.; Münck, E.; Uffelman, E. S. *J. Am. Chem. Soc.* **1990**, *112*, 5637–5639. (d) Collins, T. J.; Fox, B. G.; Hu, Z. G.; Kostka, K. L.; Münck, E.; Rickard, C. E. F.; Wright, L. J. *J. Am. Chem. Soc.* **1992**, *114*, 8724–8725. (e) Collins, T. J. *Acc. Chem. Res.* **1994**, *27*, 279–285.
(11) (a) McGaughey, G. B.; Gagné, M.; Rappé, A. K. *J. Biol. Chem.* **1998**, *273*, 15458–15463. (b) Meyer, E. A.; Castellano, R. K.; Diederich, F. *Angew. Chem., Int. Ed.* **2003**, *42*, 1210–1250.

Scheme 2

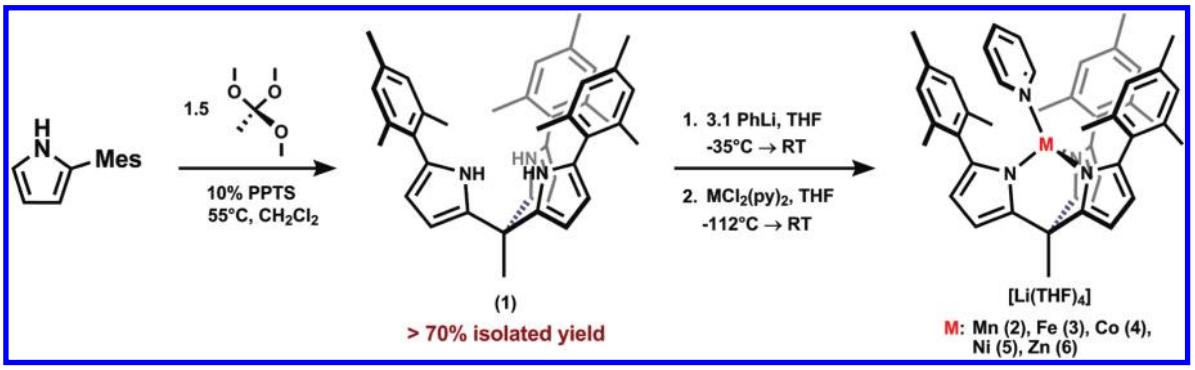

Table 1. X-Ray Diffraction Experimental Details for **2**−**6**[a,b]

	2	3	4	5	6
empirical formula	$C_{62}H_{79}LiMnN_4O_4$	$C_{62}H_{83}FeLiN_4O_4$	$C_{66}H_{87}CoLiN_4O_5$	$C_{62}H_{79}LiN_4NiO_4$	$C_{66}H_{87}LiN_4O_5Zn$
fw	1006.17	1011.11	1082.27	1009.94	1088.71
space group	*C*2/c	*C*2/*c*	$P\bar{1}$	$P2_1/n$	$P\bar{1}$
a (Å)	18.6178(9)	19.4776(12)	12.0728(7)	13.0737(17)	12.0972(8)
b (Å)	16.7236(8)	15.5448(10)	13.1443(7)	22.273(3)	13.2008(8)
c (Å)	38.7477(18)	38.314(2)	21.9752(12)	19.323(5)	21.9749(14)
α (deg)	90	90	77.5480(10)	90	77.6430(10)
β (deg)	102.5460(10)	102.561(2)	88.9730(10)	93.16(3)	89.1500(10)
γ (deg)	90	90	63.4090(10)	90	62.8850(10)
V (Å^3)	11776.3(10)	11322.8(12)	3032.6(3)	5618.1(18)	3037.3(3)
Z	8	8	2	4	2
μ (mm^{-1})	0.271	0.316	0.334	0.395	0.455
reflections	53543	49291	51355	78916	50961
completeness (to *θ*)	99.8% (26.66°)	99.9% (27.48°)	100.0% (25.03°)	99.6% (27.31°)	99.7% (28.01°)
GOF on F^2	1.041	1.012	1.034	1.019	1.035
R1, wR2[c] [I > 2*σ* (I)]	0.0534, 0.1508	0.0614, 0.1399	0.0433, 0.1187	0.0506, 0.1228	0.0526, 0.1464
$R_{indices}$ (all) (R1, wR2)	0.0663, 0.1597	0.1350, 0.1694	0.0496, 0.1253	0.0817, 0.1429	0.0634, 0.1579

[a] *λ* (Å) = 0.71073. [b] Collection temperature (*T*) = 193(2) K for **2**−**6**, 100(2) for **7**. [c] $R1 = \sum\frac{||F_o|-|F_c||}{\sum|F_o|}$, $wR2 = \left\{\frac{\sum[w(F_o^2-F_c^2)^2]}{\sum[w(F_o^2)^2]}\right\}^{1/2}$.

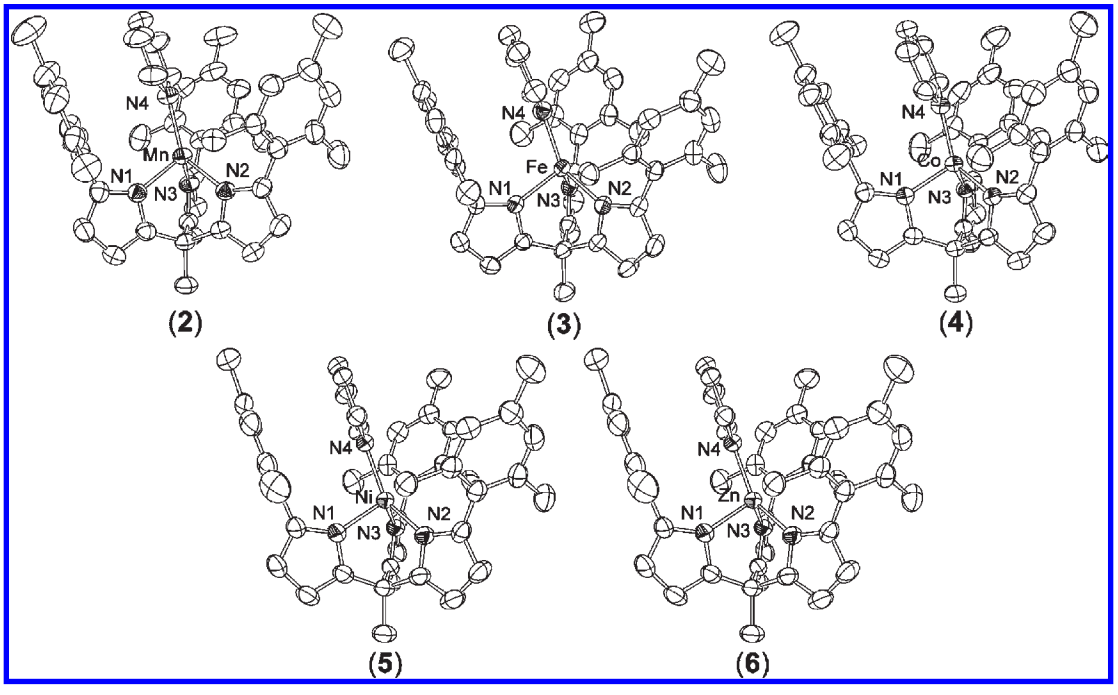

Figure 1. Solid-state molecular structure of the anions for complexes **2**−**6** with the thermal ellipsoids set at the 50% probability level (hydrogen atoms, solvated Li cations, and positional disorder in **5** are omitted for clarity).

symmetric orientation of the $M-N_{pyridine}$ bond axis. The *θ* angles listed in Table 2 show a deviation from linearity (*θ* = 157−168°). For complexes **2**−**6**, the bond lengths within the tpe ligand framework do not vary considerably

Table 2. Selected Bond Lengths (Å) and Angles (deg) for Complexes **2**−**6**

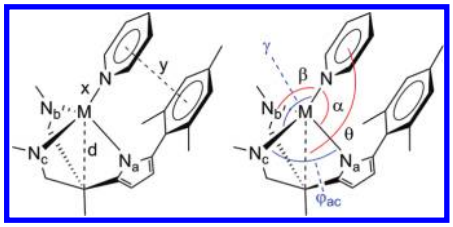

M	M−N_a	M−N_b	M−N_c	*d* (Å)	*x* (Å)	*y* (Å)	θ (deg)	α (deg)	β (deg)	γ (deg)	φ_{ab}	φ_{ac}	φ_{bc}
Mn (**2**)	2.070	2.078	2.073	2.996	2.147	4.040	168.13	114.18	134.84	120.77	92.10	93.48	90.93
Fe (**3**)	2.015	1.999	2.027	2.918	2.068	3.739	161.43	107.67	138.65	117.07	94.38	95.52	94.29
Co (**4**)	1.973	1.981	1.975	2.863	2.016	3.617	168.06	109.17	127.75	123.67	96.27	96.20	96.67
Ni (**5**)	1.960	1.955	1.989	2.935	2.040	3.528	157.95	105.74	115.20	143.96	94.33	94.76	91.87
Zn (**6**)	1.988	1.981	1.984	2.876	2.009	3.623	168.24	109.62	123.97	127.73	95.90	95.86	96.43

Table 3. Magnetic and Spectral Properties of Complexes **2**, **3**, **4**, and **5**

complex	*S*	μ_{eff} (BM)[a]	λ/nm (ε/M^{-1} cm^{-1})	δ (ΔE_q) (mm/s)
[(tpe)Mn(py)] [Li(THF)$_4$] (**2**)	5/2	6.2(1)	331 (11000), 502 (140), 477 (110)	
[(tpe)Fe(py)] [Li(THF)$_4$] (**3**)	2	5.1(1)	317 (16000), 516 (1100), 560 (920)^{sh}, 1636 (250), 1911 (180)^{sh}	0.84 (2.54)
[(tpe)Co(py)] [Li(THF)$_4$] (**4**)	3/2	4.8(1)	325 (12000), 550 (850), 621 (730), 650 (860), 998 (200), 1250 (90)^{sh}	
[(tpe)Ni(py)] [Li(THF)$_4$] (**5**)	1	2.9(1)	319 (13000), 398 (1500)^{sh}, 504 (500)^{sh}, 631 (570), 800 (120), 928 (60)	

[a] Room temperature (295 K) moment in solution by Evans method.[12]

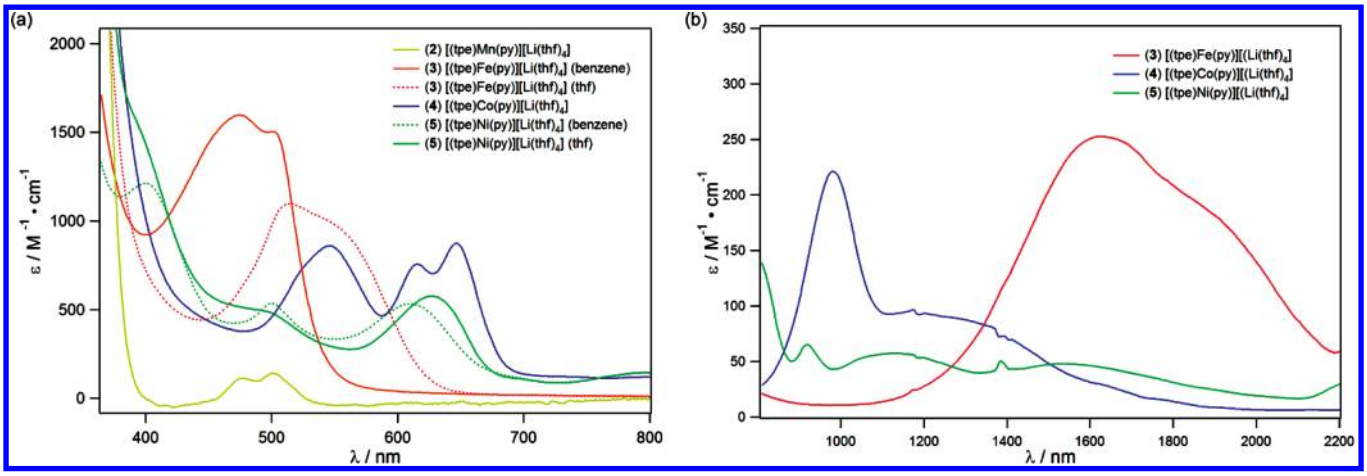

Figure 2. (a) UV/vis molar absorptivity spectra of **2**, **3** in benzene, **3** in THF, **4**, **5** in benzene, and **5** in THF and (b) NIR molar absorptivity spectra of **3**, **4**, and **5** in THF. Spectra were taken in THF (unless otherwise noted); molar absorptivities are based on measurements at a minimum of four different concentrations.

(Table S15, Supporting Information). The metal pyrrolide nitrogen bond lengths decrease across the series from Mn → Ni, with Zn being slightly elongated (d_{avg} (Å): Mn−N_{tpe} = 2.074, Fe−N_{tpe} = 2.014, Co−N_{tpe} = 1.976, Ni−N_{tpe} = 1.968, Zn−N_{tpe} = 1.984; see Table 2 for a more comprehensive comparison of bond lengths).

II.c. Electronic and Magnetic Characterization of Complexes 2−**5.** The magnetic and spectral data for complexes **2**−**5** are provided in Table 3. All four complexes feature an intense absorption in the UV region centered around 320 nm (ε/(M^{-1} cm^{-1}): 11 000−16 000) which dominate all other transitions observed. The pale yellow, ^{1}H NMR silent, high spin d^5 (S = $^5/_2$, μ_B = 6.2(1)) Mn complex **2** has only two very weak transitions in the visible region (Figure 2a, λ_{max}/nm (ε/M^{-1} cm^{-1}): 502 (140), 477 (110)), and no transitions were observed in the near-infrared region (NIR). In benzene solutions, the high spin d^6 (S = 2, μ_B = 5.1(1)) Fe complex **3** maintains its bright orange hue (λ_{max}/nm (ε/M^{-1} cm^{-1}): 505 (1500), 477 (1600)) but turns an intense magenta color upon dissolution in THF (λ_{max}/nm (ε/M^{-1} cm^{-1}): 516 (1100), 560 (920)). This significant λ_{max} shift (55 nm) could be attributable to solvent binding in THF, but we have no evidence for accessing five-coordinate structures (in solution or the solid state). The Mössbauer spectrum of **3** (Figure 6a) is best modeled as a single quadrupole doublet and parameters consistent with the Fe^{II} assignment (δ = 0.84 mm s^{-1}, $|\Delta E_Q|$ = 2.54 mm s^{-1}) in a tetrahedral ligand field. The high spin d^7 (S = $^3/_2$, μ_B = 4.8(1)), dark blue Co complex **4** shows several transitions in the visible region (λ_{max}/nm (ε/M^{-1} cm^{-1}): 550 (850), 621 (730), 650 (860)), but no solvent dependence like complex **3**. While not as

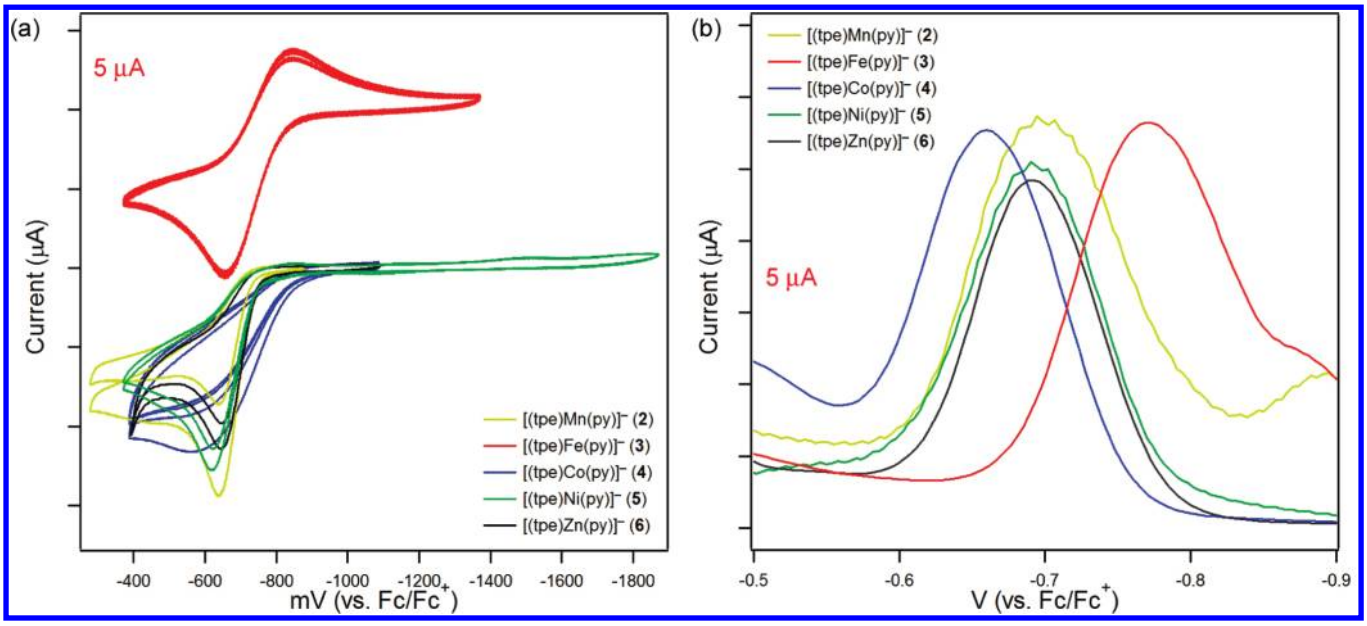

Figure 3. (a) Cyclic voltammograms of solutions in THF of 3 mM $[(tpe)M(py)]^-$ (M = Mn (**2**), Fe (**3**), Co (**4**), Ni (**5**), Zn (**6**); Bu_4NPF_6 (0.3 M); scan rate 25 mV/s on glassy C electrode). (b) Differential pulse voltammograms for solutions in THF of 10^{-4} M $[(tpe)M(py)]^-$ (M = Mn (**2**), Fe (**3**), Co (**4**), Ni (**5**), Zn (**6**); Bu_4NPF_6 (0.3 M); scan rate 25 mV/s on glassy C electrode).

Scheme 3

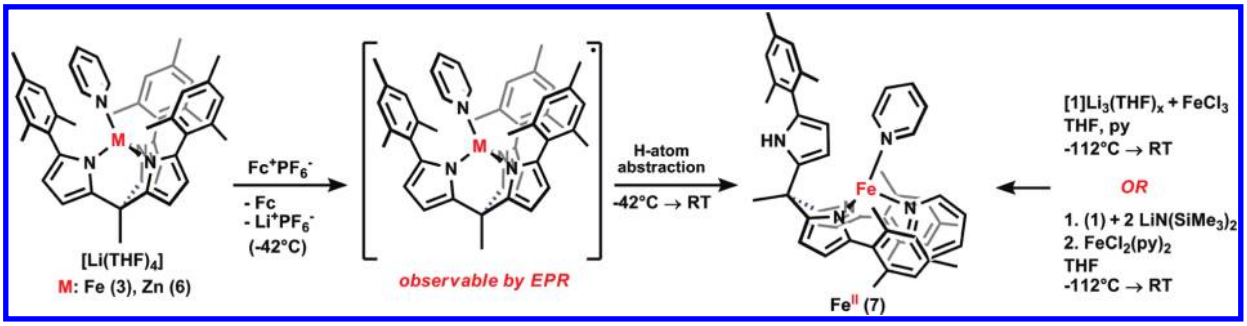

significant as **3**, the spectral features of the high spin d^8 ($S = 1$, $\mu_B = 2.9(1)$), green Ni complex **5** sharpen considerably in benzene solutions, but the gross spectral features are consistent with THF solutions (λ_{max}/nm (ε/M^{-1} cm^{-1}): 504 (500), 631 (570), 800 (120)). All of the spectral features for complexes **2**−**5** are of the appropriate magnitude for spin-allowed d−d transitions for the high spin complexes in pseudotetrahedral ligand fields. The Fe (**3**), Co (**4**), and Ni (**5**) all show very weak absorptions in the NIR region (Figure 2b) with molar absorptivities (ε = 50−250 M^{-1} cm^{-1}) substantially less than expected for charge transfer bands (e.g., LMCT).

II.d. Electrochemical Behavior of Tris(pyrrolide)ethane Complexes. Cyclic voltammetry was performed on the monopyridine complexes, **2**−**6** (0.3 M Bu_4NPF_6, Figure 3). Only the Fe complex **3** showed a quasi-reversible redox wave centered at −750 mV ($\Delta_{(EC-EA)}$ = 190 mV). Complexes **2**−**6** nearly exhibit the same onset of oxidation in the cyclic voltammetry experiments, with all of the complexes having the same peak anodic current at −655 mV (vs Fc/Fc^+). Differential pulse voltammetry measurements scanning oxidatively over the potential range of −500 to −900 mV (Figure 3b) shows that the peak anodic current for the Mn (**2**), Ni (**5**), and Zn (**6**) complexes is identical (−690 mV), whereas the Fe (**3**, −770 mV) and Co (**4**, −660 mV) complexes are slightly shifted. We interpret the redox inactive Zn^{II} data to imply the observed oxidation step is ligand-centered, originating from the tpe framework. Although the oxidations observed appear to be ligand-centered and vary little with divalent cation substitution, the onset of oxidation for metalated (tpe) shifts nearly 1.1 V from the free $(tpe)H_3$ (E_p = +375 mV).

II.e. Chemical Oxidation Products. Chemical oxidation of $[(tpe)Zn(py)][Li(THF)_4]$ (**6**) with $Fc^+PF_6^-$ did not lead to tractable products when warmed to room temperature (Fc = $(\eta^5\text{-}H_5C_5)_2Fe$). However, maintaining the reaction temperature at −42 °C in an acetonitrile/dry ice bath, we were able to observe the consumption of the ferrocenium oxidant by ^1H NMR and a detectable oxidized species by EPR (Scheme 3). Consumption of the oxidant is also apparent, as the pale yellow color of **6** quickly gives way to an intense dark brown color of the oxidized product. The EPR spectrum for this oxidation product is shown in Figure 4, which shows an isotropic signal virtually unperturbed for an organic radical (g = 2.0023).

(12) (a) Evans, D. F. *J. Chem. Soc.* **1959**, 2003–2005. (b) Sur, S. K. *J. Magn. Reson.* **1989**, *82*, 169–173.

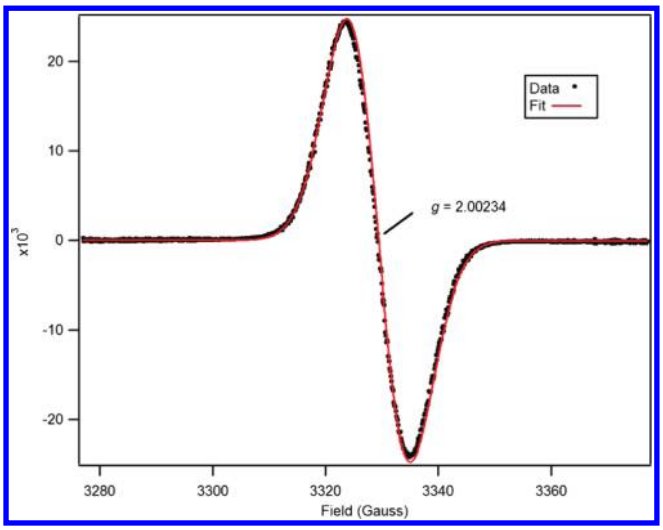

Figure 4. Toluene glass EPR of oxidation product of [(tpe)Zn(py)][Li(THF)$_4$] + $Fc^+PF_6^-$ (dotted line is experimental data and red line is data simulation: g = 2.0023, S = 1/2; 77 K, X-band, 9.3298 GHz; fit with Gaussian and Lorentzian functions).

Encouraged by the quasi-reversible nature of the electrochemical oxidation of the Fe complex **3**, we canvassed the reactivity of **3** with a range of chemical oxidants. Low temperature oxidation of **3** with $Fc^+PF_6^-$ or $NO^+SbF_6^-$ (frozen THF → room temperature) gave rise to a new paramagnetic product(s) by ^{1}H NMR. As with the oxidation of **6**, oxidation of **3** quickly changes from orange (in arene solvents) to an intense brown color upon consumption of the oxidant. This product mixture was unaffected by temperature (thawing THF, −42 °C, or room temperature) or chemical oxidant employed during the reaction. Following removal of volatiles in vacuo, extraction of the reaction mixture with diethyl ether and removal of the ferrocene by washing with copious amounts of hexanes separated the tpe-containing products. Storage of this material in diethyl ether at −35 °C gave crystals of a yellow brown material that were suitable for X-ray diffraction analysis. The molecular structure of this crystal is shown in Figure 5. In the product, one of the pyrrolide donors is not bound to the Fe, which now features two pyridine molecules giving the formulation (κ^2-tpeH)Fe(py)$_2$ (**7**). The production of **7** could be maximized by running the oxidation of **3** in a mixture of THF and pyridine as a solvent (frozen THF → RT). Authentic samples of **7** were prepared by deprotonation of (tpe)H$_3$ (**1**) with 2 equiv of LiN(SiMe$_3$)$_2$ in THF followed by the addition of FeCl$_2$(py)$_2$. Comparing the ^{1}H NMR spectrum of the crude reaction mixture from the chemical oxidation of **3** with an authentic sample of **7** confirms that **7** is the major species formed in that product mixture. Furthermore, reaction of in situ prepared (tpe)Li$_3$ with FeCl$_3$ in a mixture of pyridine and THF produced large quantities of **7** as the dominant product (Scheme 3).

Mössbauer spectroscopy on the reaction product of **3** with chemical oxidants indicated that a mixture of species was present (Figure 6b). The spectrum can be tentatively modeled as a three-component mixture with one major species (δ, $|\Delta E_Q|$ (mm·s^{-1})), component 1: 0.81, *3.27* (56.9%); component 2: 0.71, *2.21* (33.5%); component 3: 1.02, *1.51* (9.6%)). The isomer shifts and quadrupole splitting parameters are similar in nature to those for

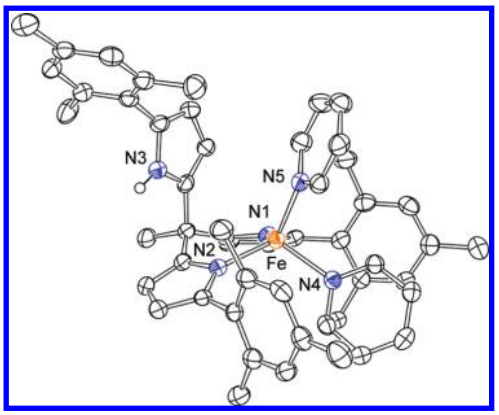

Figure 5. Solid-state molecular structure of **7** with the thermal ellipsoids set at the 50% probability level (hydrogen atoms are omitted for clarity).

complex **3**. Mössbauer analysis of an authentic sample of **7** is provided in Figure 6c, and its isomer shift and quadrupole splitting (δ, $|\Delta E_Q|$ (mm·s^{-1}): 0.81, *3.47*) match the major product from the chemical oxidation of **3** and are nearly identical for the related dipyrromethane analogue (^{Mes}dpma)Fe^{II}(py)$_2$ (δ, $|\Delta E_Q|$ (mm·s^{-1}): 0.80, *3.46*).[8] The secondary component apparent in the Mössbauer spectrum of **7** (Figure 6c) is potentially due to a geometric isomer of **7**,[13] similar to that observed in the related dipyrromethane analogue (^{Mes}dpma)Fe^{II}(py)$_2$, although the presence of two isomers could not be resolved by ^{1}H NMR spectroscopy.[8] The presence of two isomers for **7** in solution is readily apparent in the ^{1}H NMR spectra, with two sets of proton resonances obvious in analytically pure samples of **7**, where the composition was ascertained by combustion analysis. The spectrum shown in Figure 6c was obtained quickly after preparation of **7**. Mössbauer analysis on samples of **7** where both isomers are present in equal quantities by ^{1}H NMR spectroscopy show both sets of quadrupole doublets that comprise the spectrum in Figure 6c.

II.f. Density Functional Theoretical Considerations. To further probe the electronic structure of the [(tpe)M(py)]$^-$ anions **2**−**6**, geometry optimization calculations were performed (M05-2X/6-31G).[14,15] Use of the M05-2X functional was necessary in order to reproduce the pyridine/mesityl π-stacking effect observed in each of the solid-state structures for complexes **2**−**6**. Upon satisfactory optimization of the molecular geometries, a single point population analysis was performed to compute the orbital energies for complexes **2**−**6** using standard functionals and larger basis sets (B3LYP/M,N, TZV(P); all other atoms, SV(P)).[16−18] The frontier orbital energies for complexes **2**−**6** are presented in Figure 7. The orbitals

(13) Long, G. J.; Whitney, D. L.; Kennedy, J. E. *Inorg. Chem.* **1971**, *10*, 1406–1410.
(14) (a) Zhao, Y.; Schultz, N. E.; Truhlar, D. G. *J. Chem. Theory Comput.* **2006**, *2*, 364–382. (b) Zhao, Y.; Truhlar, D. G. *Acc. Chem. Res.* **2008**, *41*, 157–167.
(15) Ditchfield, R.; Hehre, W. J.; Pople, J. A. *J. Chem. Phys.* **1971**, *54*, 724–728.
(16) (a) Becke, A. D. *J. Chem. Phys.* **1993**, *98*, 5648–5652. (b) Vosko, S. H.; Wilk, L.; Nusair, M. *Can. J. Phys.* **1980**, *58*, 1200–1211. (c) Lee, C.; Yang, W.; Parr, R. G. *Phys. Rev. B* **1988**, *37*, 785–789.
(17) Schäfer, A.; Huber, C.; Ahlrichs, R. *J. Chem. Phys.* **1994**, *100*, 5829–5835.
(18) Schäfer, A.; Horn, H.; Ahlrichs, R. *J. Chem. Phys.* **1992**, *97*, 2571–2577.

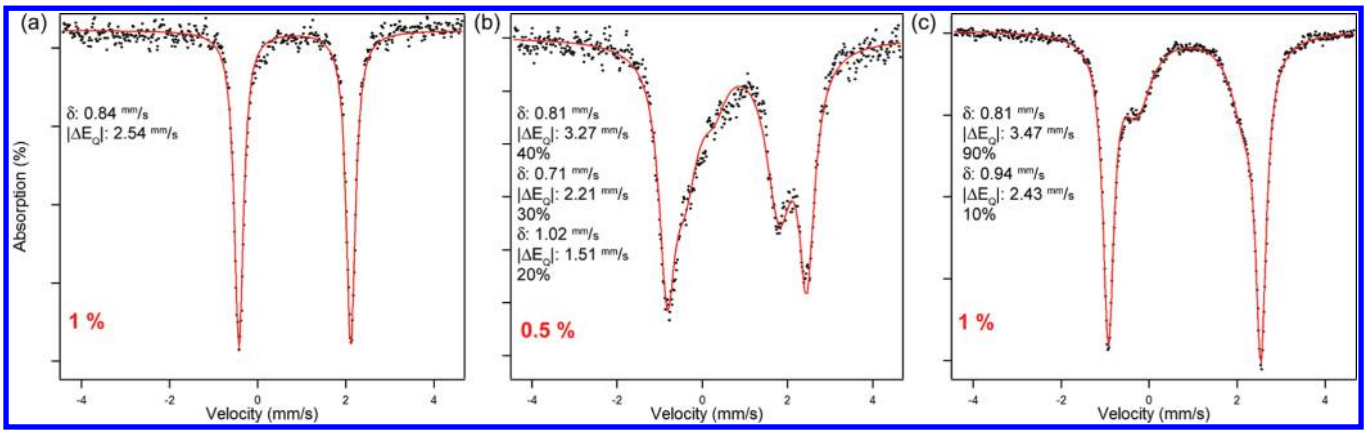

Figure 6. Mössbauer spectrum of (a) [(tpe)Fe(py)][Li(THF)$_4$] (**3**) at 77 K (δ, $|\Delta E_Q|$ (mm s^{-1}): 0.84, *2.54*); (b) oxidation product of **3** with $Fc^+PF_6^-$, at 77 K (δ, $|\Delta E_Q|$ (mm s^{-1}), component 1: 0.81, *3.27* (56.9%); component 2: 0.71, *2.21* (33.5%); component 3: 1.02, *1.51* (9.6%)); (c) (κ^2-tpe)Fe(py)$_2$ (**7**) at 77 K (δ, $|\Delta E_Q|$ (mm s^{-1}), component 1: 0.81, *3.47* (80.6%); component 2: 0.94, *2.43* (19.4%)).

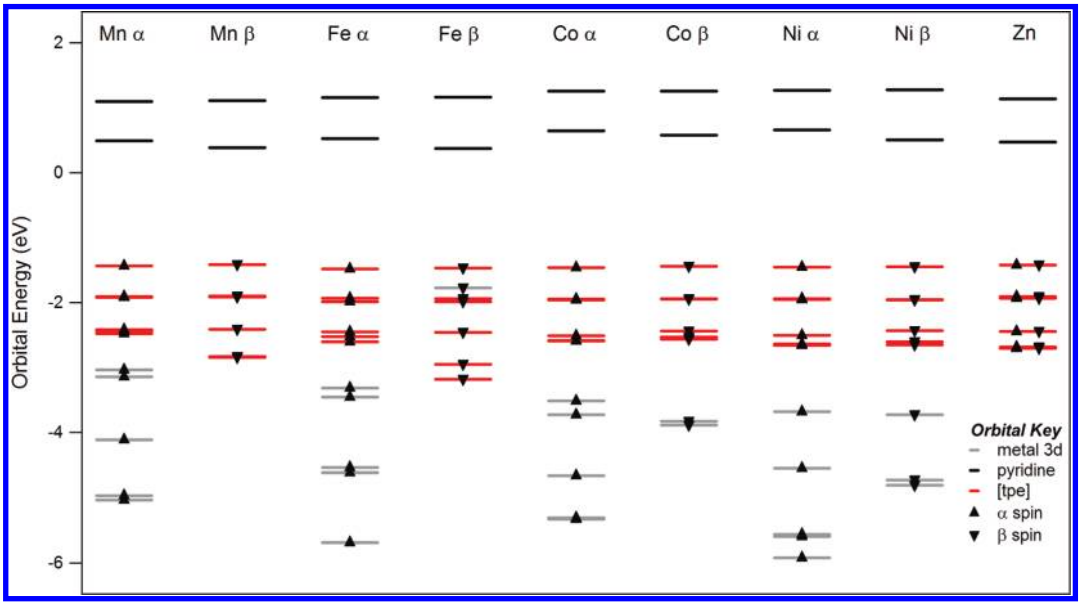

Figure 7. Calculated α (▲) and β (▼) orbital energies for [(tpe)M(py)]$^-$ complexes: Mn (**2**, 5 α), Fe (**3**, 5 α, 1 β), Co (**4**, 5 α, 2 β), and Ni (**5**, 5 α, 3 β). Calculated restricted molecular orbitals for [(tpe)Zn(py)]$^-$ (**6**). Metal-based orbitals are gray, tris(pyrrolyl)ethane ligand-based orbitals are red (6 α, 6 β for **2**−**5**), and pyridine-based orbitals are black.

originating from the tpe ligand are shown in red, metal 3d orbitals in gray, and pyridine orbitals in black. In every instance, the Mulliken population analysis (MPA) calculations indicate the highest lying occupied molecular orbitals (HOMO, HOMO-1) exclusively feature ligand π-character on the pyrrole subunits, illustrated for complex **3** in Figure 8. Across the series, the metal 3d orbitals do not significantly contribute to the frontier orbitals until HOMO-4, approximately 1.5 eV lower in energy than the ligand-based HOMO. Only the Fe complex **3** shows a significant component of metal 3d orbital contribution to the frontier orbitals in the β population. The spin density plot (α−β) for the Fe complex (Figure 9d) shows that all of the unpaired spin is localized on the metal ion, which is consistent for all the open-shell molecules examined (**2**, **4**, and **5**; Figure S2−S4, Supporting Information).

We also probed the structure of the oxidation products for the Zn and Fe anions by density functional methods. The geometries for the oxidized complexes (tpe)Zn(py) ($S = {}^1/_2$, **8**) and (tpe)Fe(py) ($S = {}^5/_2$, **9**) were optimized using the optimized structure data of **6** and **3** as starting points, respectively. The geometry optimization of (tpe)-Fe(py) with $S = {}^3/_2$ was also examined but failed to converge using standard convergence criteria. The total energy of both optimized structures for the oxidation products was higher in energy (**8**, +2.531 eV; **9**, +2.465 eV) than the geometry minimized structures for the corresponding anions. The calculated α and β orbital energies presented in Figure 9b and e were offset by these energy differences to correct for the overall structural zero-point energy differences. In both instances, the new HOMO−LUMO gaps (1.2 eV for oxidized Zn and Fe products) were substantially lower than those calculated for **6** (1.9 eV) or **3** (2.2 eV). The calculated spin densities (α−β) for the oxidation products of **6** and **3** are shown in Figure 9c and f, respectively. The resultant radical density for the $S = {}^1/_2$ (tpe)Zn(py) is contained entirely within the tpe framework, consistent with organic-radical-like EPR spectrum (Figure 4) observed for the oxidation product.

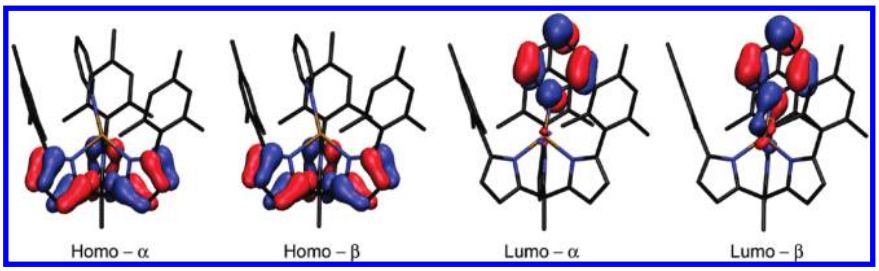

Figure 8. HOMO (α and β) and LUMO (α and β) from frontier orbital diagrams for complex **3** (Fe, $S = 2$) by DFT (B3LYP/TZV(P), SV(P); Gaussian 03).

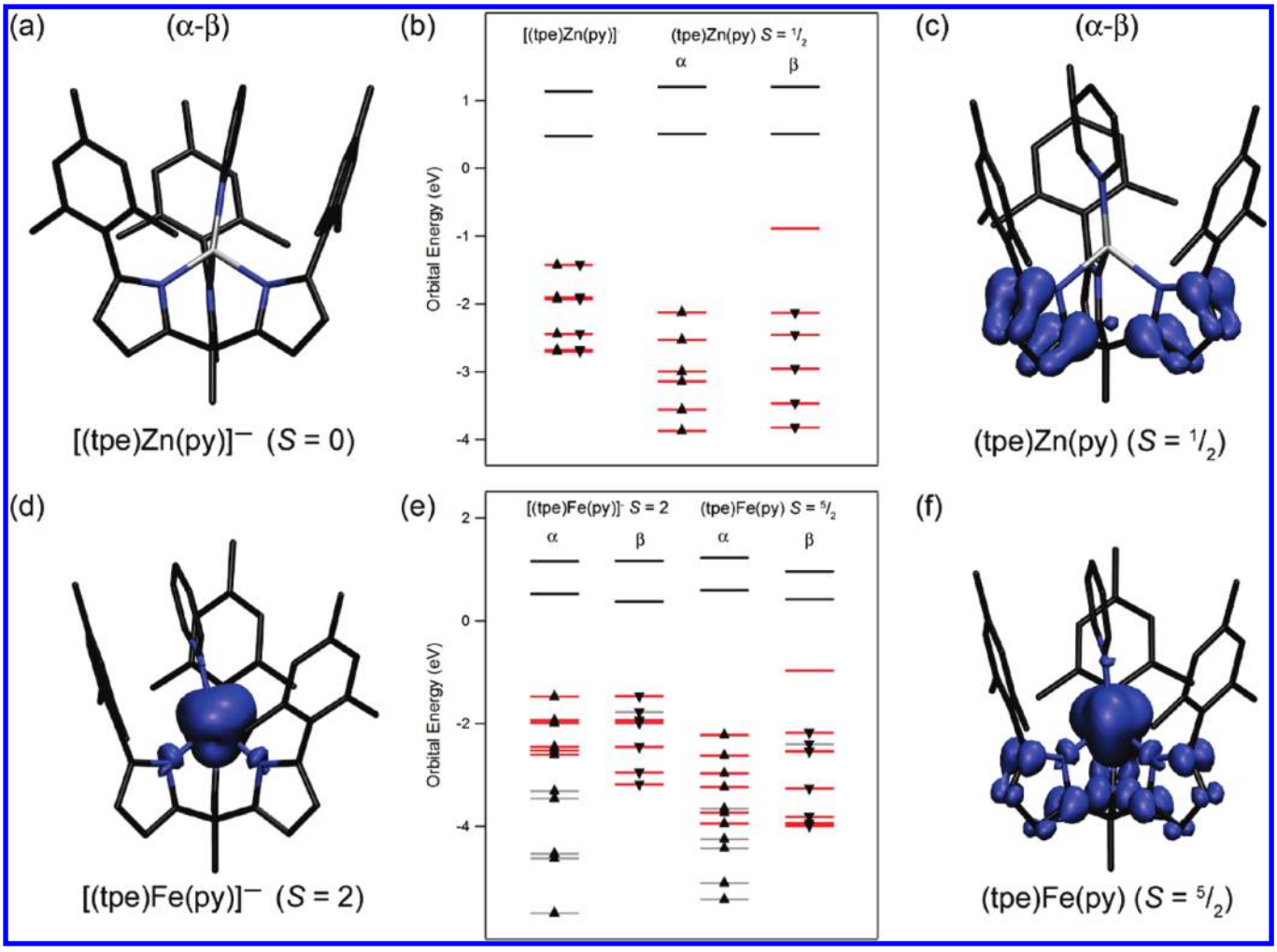

Figure 9. Calculated spin population (α−β) for (a) $[(tpe)Zn(py)]^-$ ($S = 0$), (c) (tpe)Zn(py) ($S = {}^1/_2$), (d) $[(tpe)Fe(py)]^-$ ($S = 2$), and (f) (tpe)Fe(py) ($S = {}^5/_2$). (b) Molecular orbitals for $[(tpe)Zn(py)]^-$ and calculated α (▲) and β (▼) orbital energies for the oxidation product (tpe)Zn(py) ($S = {}^1/_2$). (e) Calculated α (▲) and β (▼) orbital energies for $[(tpe)Fe(py)]^-$ ($S = 2$) and the oxidation product (tpe)Fe(py) ($S = {}^5/_2$) by DFT (B3LYP/TZV(P), SV(P); Gaussian 03).

Similarly, the calculated spin density for the oxidation product (tpe)Fe(py), assuming an $S = {}^5/_2$ ground state, now shows considerable ligand contribution (Figure 9f), whereas the spin is localized completely on the Fe ion for **3** (Figure 9d).

III. Discussion

III.a. [(tpe)M(py)]⁻ Structural Considerations. The tpe ligand framework is a rigid, tripodal framework that sterically enforces a pseudotetrahedral coordination environment about the bound transition metal ion. Accordingly, this class of complexes is related to other "tetrahedral enforcer" ligands (e.g., tris(^{R}L)borates[19−21]) but differs in that it coordinates transition-metals as a trianionic species. The N_{tpe}−M bond lengths decrease across the series from Mn → Ni, which is consistent with the decreasing high-spin ionic radius for the series. The pyridine ligand is not bound along the 3-fold axis of symmetry (i.e., axis depicted "d" in the diagram for Table 2) for any of the molecules reported, even for the

(19) (a) Trofimenko, S. *J. Am. Chem. Soc.* **1966**, *88*, 1842–1844. (b) Trofimenko, S. *Chem. Rev.* **1993**, *93*, 943–980.
(20) Byers, P. K.; Canty, A. J.; Honeyman, R. T. *Adv. Organomet. Chem.* **1992**, *34*, 1–65.

d^5 Mn (**2**) and d^{10} Zn (**6**) complexes where steric minimization should dominate bonding. Instead, the pyridine is bound well off-axis, positioned in a π-stacking orientation with one of the ligand mesityl fragments, resulting in a trigonal monopyramidal geometry instead of a tetrahedral arrangement. The pyridine−mesityl separation (3.5−4.0 Å) is within π-stacking distances reported in the literature and is estimated to provide an additional 1−2 kcal/mol of energy to the stabilization of the ground state.[11] While the pyridine binding off-axis could maximize the π overlap between the metal d orbitals (i.e., 2e set for a ML_3 fragment) and the pyridine π-accepting orbitals,[22] the π back-bonding contribution to the M−pyridine binding should be quite minimal for the high-spin, 3d M^{2+} ions examined, and therefore the π-stacking interaction is the most likely cause for deviation from the expected pseudo-C_{3v} geometry.

III.b. Electronic Structure. In our studies of the redox properties of the related dipyrromethane metal complexes of the type (^{Mes}dpma)M(py)$_2$, we observed matching of the ligand-based orbitals with the frontier metal orbitals similar to the tpe system presented here.[8] We considered three possible scenarios regarding potential intramolecular redox for those systems which are relevant to consider when evaluating the electronic structure of the current tpe frameworks: (1) high-energy pyrrole-based electrons reduce the bound metal ion with n e^-, leaving n holes on the ligand platform (i.e., $(L^0)M^{2+} \rightarrow (L^{n+})M^{2-n}$); (2) the ligand and metal 3d orbitals are close enough in energy such that spin-state tautomerism is possible;[23] (3) no intramolecular redox occurs, leaving each metal in the divalent state and the ligand in a fully reduced, closed-shell configuration.

Scenario 1. If scenario 1 was operative, we would anticipate a stepwise elongation of the pyrrole subunits within the tpe framework across the 3d series from oxidation of the ligand framework. No ligand metrical perturbations to suggest this are apparent when comparing the structural data for complexes **2**−**6** (Table S15, Supporting Information). In addition, the UV−vis absorption spectra do not reveal any readily assignable ligand-to-metal charge-transfer bands that would suggest the presence of excited states consistent with this scenario. The only absorption band of appropriate intensity ($\lambda \approx$ 320 nm, $\varepsilon > 10^4$ M^{-1} cm^{-1}) corresponds to a ligand-to-ligand charge transfer band that is present in the deprotonated ligand (tpe)Li_3 (λ_{max} = 313 nm, ε = 9000 $M^{-1}cm^{-1}$; Figure S1, Supporting Information). Furthermore, calculations on the oxidation product of **6** ((tpe)Zn(py), **8**) provide an estimate of the energetic cost in excess of 2 eV ($\Delta E = E_{tot}(\mathbf{6}) - E_{tot}(\mathbf{8})$) toward oxidation of the tpe framework, suggesting an intramolecular redox transfer should be energetically disfavored.

Scenario 2. Each of the complexes from Mn (**2**) to Ni (**5**) feature high-spin configurations which are evident by the low temperature X-ray diffraction studies (193 K), low temperature Mössbauer for **3** and **7**, and the room temperature solution magnetic moment determinations for complexes **2**−**5** (Table 3). This is especially notable for M = Ni (**5**), which in the dipyrromethane system is found to be square planar and diamagnetic.[8] The DFT spin density analyses of **2**−**5** suggest that all spin is localized on the corresponding 3d ion without significant contribution from the ligand (Figure 9; Figures S2−4, Supporting Information). These data imply that no spin-state tautomerism is occurring. If the oxidation of the tpe framework is as energetically disfavored as estimated by DFT, this suggests a considerable barrier for spin-state tautomerism.

Scenario 3. On the basis of the evidence we have collected, we have determined that metal complexes of the tpe trianion fall into scenario 3, where the available redox reservoirs (i.e., tpe, 3d metal ion) are well separated and do not show any evidence for intramolecular redox transfer in the outer-sphere electron transfer reactions, as also observed in the dipyrromethane system we previously reported.[8] This feature is most obvious in the electrochemical behavior of complexes **2**−**6**, both in the cyclic and differential pulse voltammetry experiments (Figure 3), which suggest that the $[(tpe)M(py)]^-$ species traverse a similar oxidation pathway regardless of the metal ion present or its spin-multiplicity. The commonality of the electrochemical oxidations, EPR on the oxidation product of **6**, and the DFT results indicate the kinetic products of the one-electron oxidation reactions are ligand-centered radicals, rather than metal-centered oxidations (eq 1):

$$[(tpe)M^{II}(py)]^- \xrightarrow{-e^-} [(tpe^{\bullet+})M^{II}(py)] \xrightarrow[+L]{\text{H-atom abstraction}} [(\kappa^2\text{-tpe})M^{II}(py)(L)] \quad (1)$$

Both cyclic and differential pulse voltammetry exhibit multiple oxidation events following the primary oxidation highlighted in Figure 3. Unlike the dipyrromethane analogues previously reported, we do not observe the multielectron redox events attributable to a one-electron oxidation of each of the pyrrolide subunits. The primary, irreversible oxidation of the $[(tpe)M(py)]^-$ anions produces a dipyrromethane-like product (κ^2-tpe)M(py)(L) following H-atom abstraction from the ($tpe^{\bullet+}$)M(py) intermediate. The source of H atoms is likely THF, either bound to lithium or in the solvent. Experiments with dihydroanthracene as a sacrificial H-atom donor showed no anthracene formation. The onset of oxidation for the dipyrromethane complexes of the formulation (^{Mes}dpma)M(py)$_2$ does not occur until −240 mV (vs Fc/Fc^+).[8] Thus, the secondary redox event for the $[(tpe)M(py)]^-$ anions is not anticipated to occur until a similar potential, separated from the initial oxidation by nearly 450 mV.

(21) (a) Tris(alkylthiol)borate: Ge, P.; Haggerty, B. S.; Rheingold, A. L.; Riordan, C. G. *J. Am. Chem. Soc.* **1994**, *116*, 8406−8407. (b) Schebler, P. J.; Mandimutsira, B. S.; Riordan, C. G.; Liable-Sands, L. M.; Incarvito, C. D.; Rheingold, A. L. *J. Am. Chem. Soc.* **2001**, *123*, 331–332. (c) Tris(alkylphosphino)borates: Peters, J. C.; Feldman, J. D.; Tilley, T. D. *J. Am. Chem. Soc.* **1999**, *121*, 9871−9872. (d) Barney, A. A.; Heyduk, A. F.; Nocera, D. G. *Chem. Commun.* **1999**, 2379–2380. (e) Betley, T. A.; Peters, J. C. *Inorg. Chem.* **2003**, *42*, 5074–5084. (f) Thomas, C. M.; Mankad, N. P.; Peters, J. C. *J. Am. Chem. Soc.* **2006**, *128*, 4956−4957. Tris(carbeno)borates:(g) Nieto, I.; Cervantes-Lee, F.; Smith, J. M. *Chem. Commun.* **2005**, 3811–3813. (h) Cowley, R. E.; Bontchev, R. P.; Duesler, E. N.; Smith, J. M. *Inorg. Chem.* **2006**, *45*, 9771–9780.

(22) (a) Albright, T. A.; Burdett, J. K.; Whangbo, M.-H. *Orbital Interactions in Chemistry*; John Wiley & Sons, Inc: New York, 1985; pp 381−389. (b) Detrich, J. L.; Konečný , R.; Vetter, W. M.; Doren, D.; Rheingold, A. L.; Theopold, K. H. *J. Am. Chem. Soc.* **1996**, *118*, 1703–1712.

(23) Storr, T.; Verma, P.; Pratt, R. C.; Wasinger, E. C.; Shimazaki, Y.; Stack, T. D. P. *J. Am. Chem. Soc.* **2008**, *130*, 15448–15459.

Chemical oxidation of both **3** and **6** initially produces highly colored intermediates consistent with the decreased HOMO−LUMO gap predicted for the oxidized products by DFT. The rapidity with which the unshielded tpe ligand radical abstracts $H^{\bullet}$ from solvent to produce the (κ^2-tpe)M(py)(L) species (L = pyridine or solvent) prevented isolation of the putative ($tpe^{\bullet+}$)M^{II}(py) oxidation product. The resulting coordination change at the metal accounts for the irreversibility of the cyclic voltammetry experiments. Attempted metalation of the tpe trianion with Fe^{III} sources leads to formation of the same κ^2 species in **7**. While we cannot definitively rule out intramolecular electron transfer from the tpe to Fe^{III} following ligation, the tpe trianion is a strong enough reductant to reduce the Fe^{III} precursor, and this process likely precedes halide metathesis. Extending our analysis of these observations to the dipyrromethane system, the ligand-centered oxidation processes we observed likely produced pyrrole-dissociated species, making identification of chemically oxidized materials impossible.[8]

The orbital analysis (Figure 7) for the tpe complexes shows that the energetically most accessible orbital density is localized on the tpe scaffold. The frontier orbitals consist entirely of the pyrrolide π system. This produces an apparent non-Aufbau arrangement of electrons, where fully populated ligand orbitals are higher in energy than the partially filled metal 3d orbitals. We interpret this to suggest that electron pairing in the delocalized, ligand-based π orbitals incurs less Coulombic repulsion than pairing electrons in the comparatively smaller 3d orbitals. However, the corresponding 3d β orbitals may, in fact, lie higher in energy than the ligand-based orbitals, which would not violate the Aufbau principle.[24] From a qualitative standpoint, the electronic structures predicted by DFT corroborate our experimental results, wherein outer-sphere electron transfer is dominated by the ligand π electrons.

As shown by Floriani and Floriani-Moro[4a] and Swartz and Odom,[7c] more electrophilic, early transition metal complexes bind pyrrolide subunits through an η^5 π association preferentially to terminal *N* ligation, even in porphyrinogen complexes. For iron-porphyrinogens,[4c] these same π electrons cause an intimate coupling between the metal and ligand oxidation states when orbitals of appropriate π symmetry are allowed to mix but become a liability due to their energetic accessibility when this conjugation is broken.[8] For dipyrromethane and tris(pyrrolyl)ethane systems, the highest-lying ligand orbitals do not feature any π density on the pyrrole N, making the ligands poor candidates to function as π donors to metals that could function as π acceptors. This property, coupled with the high-spin, pseudotetrahedral nature of the dipyrromethane and tris(pyrrolyl)ethane complexes, functions to make the pyrrolide and 3d ions completely decoupled redox entities. This does not rule out the two redox reservoirs engaging in cooperative redox transfer in oxidations involving two or more electrons, a process which plays a key role in stabilizing the high-valent ferryl species in cytochrome P450[25] and potentially in related tris(pyrrolyl)amine systems.[26] Work is currently underway to determine the ability of $[(tpe)ML_n]^-$ anions to function as atom or group transfer accepting platforms via metal-centered redox chemistry without being short-circuited by intramolecular redox transfer.

IV. Conclusions

We have investigated transition metal complexes of the tris(pyrollyl)ethane ligand and found them to exhibit unusual electronic properties attributable to the pyrrolide ligand framework. Electrochemical investigations on the $[(tpe)M^{II}(py)]^-$ series reveal a common irreversible oxidation pathway that is entirely ligand-based, invariant to the divalent metal bound. This observation indicates that fully populated, ligand-based π orbitals from the tpe construct are energetically most accessible, akin to their dipyrromethane analogues. DFT calculations on the anions suggest electrons pair preferentially in the higher-energy, delocalized ligand π orbitals rather than pairing within the lower-energy metal-ion 3d orbitals (e.g., in the event of an intramolecular redox transfer). This can be attributed to larger electron-pairing energy costs for the metal-based 3d orbitals. While the energetic overlap between the tpe ligand-based π orbitals and the d-orbital manifold is favorable for cooperative redox, the two redox reservoirs display totally disparate redox behavior. A major criterion for coupling ligand and transition metal redox is to have a pathway by which the two reservoirs can communicate, typically through conjugation of the ligand π orbital with d orbitals of appropriate symmetry. DFT studies reveal the tpe platform, and by extension the dipyrromethane ligand systems, do not feature frontier π-orbital density on the ligand *N* termini, shielding the ligand-based, highest occupied molecular orbitals from conjugation with the metal 3d orbitals. As a result, the ligand redox behavior observed is devoid of transition metal influence. In the context of outer-sphere electron transfer chemistry, the pyrrolic π electrons become a liability to the complex stability. These ligand platforms, however, could find significant utility in the stabilization of inner-sphere electron transfer reactivity and the resulting high-oxidation state metal complexes if L → M π contribution can be maximized.

V. Experimental Section

All manipulations were carried out in the absence of water and dioxygen using standard Schlenk techniques, or in an MBraun inert atmosphere drybox under a dinitrogen atmosphere. All glassware was oven-dried for a minimum of 1 h and cooled in an evacuated antechamber prior to use in the drybox. Benzene, diethyl ether, dichloromethane, *n*-hexane, tetrahydrofuran, and toluene were dried and deoxygenated on a Glass Contour System (SG Water USA, Nashua, NH) and stored over 4 Å molecular sieves (Strem) prior to use. Benzene-d_6 was purchased from Cambridge Isotope Laboratories and degassed and stored over 4 Å molecular sieves prior to use. Pyridinium *p*-toluenesulfonate, ferrocenium hexafluorophosphate, dihydroanthracene, and anhydrous pyridine were purchased from Aldrich and used as received. Anhydrous manganese(II), iron(II), cobalt(II), and nickel(II) chlorides were purchased from Strem and used as received. Phenyllithium was prepared by lithiation of iodobenzene

(24) Wang, L.-P.; Van Voorhis, T. Personal communication.
(25) Shaik, S.; Kumar, D.; De Visser, S. P.; Altun, A.; Thiel, W. *Chem. Rev.* **2005**, *105*, 2279−2328 and references therein.
(26) Harman, W. H.; Chang, C. J. *J. Am. Chem. Soc.* **2007**, *129*, 15128–15129.

with *n*-butyllithium. 2-(2,4,6-Trimethylphenyl)-1H-pyrrole was synthesized according to literature procedures.[27] Metal precursors $MCl_2(py)_2$ (M = Mn, Fe, Co, Ni) were synthesized on the basis of literature procedures.[13,28] Celite 545 (J. T. Baker), silica gel 32−63 μ (Dynamic Adsorbents, Atlanta, GA), 4 Å molecular sieves, tetra-*n*-butylammonium hexafluorophosphate (Alfa Aesar), and zinc chloride (Aldrich) were dried in a Schlenk flask for 24 h under a dynamic vacuum while heating to at least 150 °C.

Characterization and Physical Measurements. UV/visible spectra were recorded on a Varian Cary 50 UV/Visible spectra, with a scan rate of 300 nm/min. NIR spectra were recorded on a Varian Cary model 5000 UV−vis−NIR spectrophotometer. ^{1}H and ^{13}C NMR spectra were recorded on Varian Mercury 400 MHz or Varian Unity/Inova 500 MHz spectrometers. ^{1}H and ^{13}C NMR chemical shifts are reported relative to $SiMe_4$ using the chemical shift of residual solvent peaks as a reference. Solution magnetic susceptibilities were determined by Evans's method[12] using hexamethyldisiloxane as an internal reference. Mass spectrometry was performed at the Harvard University FAS Center for Systems Biology Mass Spectrometry and Proteomics Resource Laboratory on an Agilent 6210 TOF LC/MS with a dual nebulizer ESI source. Elemental analyses were carried out at Complete Analysis Laboratories, Inc. (Parsippany, NJ).

Electrochemical experiments were carried out using a CH Instruments CHI660C Electrochemical Workstation. The electrolyte used was 0.3 M (^{n}Bu$_4$N)(PF_6) in THF. The concentration of all analytes was 3 mM. The working electrode was glassy carbon. A platinum wire was used as the counter electrode, and nonaqueous Ag/Ag^+ reference electrodes (10 mM $AgNO_3$ in THF) were used with the corresponding electrolyte solution. Cyclic voltammetry was performed with a scan rate between 500 mV/s and 25 mV/s.

X-band EPR spectroscopic measurements were performed using a Bruker EMX spectrometer equipped with 13 in. magnets, an ER 4102ST cavity, and a Gunn diode microwave source. Samples in a toluene glass were cooled using a liquid nitrogen coldfinger dewar. Simulation and fitting of EPR data was done with the EasySpin 3.0.0[29] ToolBox for MATLAB R2008a.[30] ^{57}Fe Mössbauer spectra were measured with a constant acceleration spectrometer (SEE Co, Minneapolis, MN). Isomer shifts are quoted relative to Fe metal at room temperature. Data were analyzed and simulated with Igor Pro 6 software (WaveMetrics, Portland, OR) using Lorentzian fitting functions.

X-Ray Crystallography Procedures. All structures were collected on either a Siemens or Bruker three-circle platform goniometer equipped with either a Bruker Apex I or Apex II CCD and an Oxford cryostream cooling device. Radiation was from a graphite fine focus sealed tube Mo Kα (0.71073 Å) source. Crystals were mounted on a cryoloop using Paratone-*N* oil. Structures were collected at 193 K (**2**−**6**) and 100 K (**7**). Data were collected as a series of φ and/or ω scans. Data were integrated using SAINT (Bruker AXS) and scaled with a multiscan absorption correction using SADABS (Bruker AXS). The structures were solved by direct methods or Patterson maps using SHELXS-97[31] and refined against F^2 on all data by full matrix least-squares with SHELXL-97. All non-hydrogen atoms were refined anisotropically. Hydrogen atoms were placed at idealized positions and refined using a riding model. The isotropic displacement parameters of all hydrogen atoms were fixed to 1.2 times the *U* value of the atoms they are linked to (1.5 times for methyl groups). In all structures with a Li^+ countercation, the ligated solvent THF and ether often exhibited positional disorder, and similarity restraints were used to refine the model. Except in certain cases (as noted below), the major component of the disordered THF refined to between 54% and 95%. Further details on several structures are noted below. Note on **2**: Similarity restraints and distance and angle restraints were insufficient for refinement of residual electron density, most likely a heavily disordered free THF molecule, found in the crystal structure. The SQUEEZE function of PLATON[32] was used to remove the electron density. Details can be found in the .cif file for the structure of **2**. Note on **5**: The pyridine bound to nickel exhibited positional disorder, which was modeled using similarity and flat restraints. The major component refined to 90%. Notes on **6**: One THF-ligated to Li^+ was modeled using three positional disorders, with components of 40%, 37%, and 23%, again using similarity restraints to aid in refinement. In addition, a free THF molecule was disordered over two positions and refined with the aid of similarity restraints, with the major contributor refining to 55%. Note on **7**: The hydrogen atom bound to the nitrogen of the free pyrrole arm was explicitly located as a Q peak in the refinement and refined semifreely using restraints.

5,5′,5″-(Ethane-1,1,1-triyl)tris(2-mesityl-1H-pyrrole) (tpeH_3) (1). A 100 mL bomb flask was charged with 2-(2,4,6-trimethylphenyl)-1H-pyrrole (3.468 g, 18.72 mmol), trimethylorthoacetate (1.194 g, 9.94 mmol), and 20 mL of CH_2Cl_2. After stirring for 5 min, pyridinium *p*-toluenesulfonate (0.170 g, 0.675 mmol) was added, resulting in a color change from tan to magenta. The reaction was stirred at 55 °C for 41 h. Additional pyridinium *p*-toluenesulfonate (0.168 g, 0.668 mmol) was added, and the reaction was stirred at 50 °C for an additional 72 h. The reaction mixture was then filtered through a silica gel plug, washing with excess CH_2Cl_2 (~50 mL). Solvent and volatiles were removed in vacuo, and the resulting green-brown, sticky solid was redissolved in minimal CH_2Cl_2. Hexanes were added until a precipitate was observed, and the solution was placed into the freezer for 2 h. The precipitate was collected on a glass frit. The recrystallization procedure was repeated twice, affording **1** as an off-white powder (2.5204 g, 70%). ^{1}H NMR (300 MHz, C_6D_6): δ/ppm 7.33 (br s, 3 H), 6.82 (s, 6 H), 6.17 (t, J = 3.2 Hz, 3 H), 6.05 (t, J = 2.9 Hz, 3 H), 2.19 (s, 9 H), 2.16 (s, 16 H), 1.81 (s, 3 H). ^{13}C {^{1}H} NMR (125 MHz, C_6D_6): δ/ppm 138.8, 137.7, 136.7, 131.8, 129.9, 128.8, 108.5, 107.1, 41.3, 28.5, 21.5, 21.2. HRMS (ESI^+) m/z for $C_{41}H_{46}N_3^+$ $[M + H]^+$, calcd 580.36915. Found: 580.36933.

[(tpe)Mn(py)][Li(THF)$_4$] (2). In separate 20 mL scintillation vials, **1** (448 mg, 0.772 mmol) and PhLi (202 mg, 2.413 mmol) were each dissolved in 3 mL of THF and cooled in a −35 °C freezer. The cold solution of **1** was added to the PhLi solution and stirred at room temperature for 30 min. In another 20 mL vial, $MnCl_2(py)_2$ (220 mg, 0.775 mmol) was slurried in 3 mL of THF with ~0.5 mL of pyridine. The vials containing deprotonated **1** and $MnCl_2(py)_2$ were placed in a liquid nitrogen cooled cold well until frozen. The solution of **1** was thawed and added to the stirring slurry of $MnCl_2(py)_2$. The reaction mixture became a yellow solution as it warmed. The reaction was stirred at room temperature overnight. Removal of the solvent in vacuo gave a dark yellow residue. The residue was extracted into 5 mL of benzene and filtered through a Celite plug to remove lithium chloride. Removal of the solvent in vacuo gave a yellow powder (522.4 mg, 67%). Crystals suitable for X-ray diffraction were grown from a vapor diffusion of Et_2O into a THF solution of **2**

(27) Reith, R. D.; Mankad, N. P.; Calimano, E.; Sadighi, J. P. *Org. Lett.* **2004**, *6*, 3981–3983.
(28) Allan, J. R.; Brown, D. H.; Nuttall, R. H.; Sharp, D. W. A. *J. Chem. Soc. A* **1966**, 1031–1034.
(29) Stoll, S.; Schweiger, A. *J. Magn. Reson.* **2006**, *178*, 42–55.
(30) *MATLAB R2008a*; The MathWorks: Natick, MA, 2008.
(31) (a) Sheldrick, G. M. *Acta Crystallogr.* **1990**, *A46*, 467–473. (b) Sheldrick, G. M. *SHELX-97*; University of Göttingen: Göttingen, Germany, 1997.
(32) The Platon Homepage. http://web.mit.edu/platon_v40505/platon/docs/platon/pl000000.html (accessed Jan 2010).

at room temperature. The compound gave no signal by ^{1}H NMR. UV/vis (THF) λ_{max}/nm (ε/M^{-1} cm^{-1}): 331 (11 000), 502 (140), 477 (110). μ_{eff} (C_6D_6, 295 K): 6.2(1) μ_B. Comb. Anal. for $[C_{46}H_{47}MnN_4]^-[LiC_{16}H_{32}O_4]^+$, Calcd: C, 74.01; H, 7.91; N, 5.57. Found: C, 73.93; H, 7.74; N, 5.46.

[(tpe)Fe(py)][Li(THF)$_4$] (3). In separate 20 mL scintillation vials, **1** (246.2 mg, 0.425 mmol) and PhLi (114 mg, 1.36 mmol) were each dissolved in 3 mL of THF and cooled in a −35 °C freezer. The cold solution of **1** was added to the PhLi solution and stirred at room temperature for 30 min. In another 20 mL vial, $FeCl_2(py)_2$ (121.3 mg, 0.426 mmol) was slurried in 3 mL of THF. The vials containing deprotonated **1** and $FeCl_2(py)_2$ were placed in a liquid nitrogen cooled cold well until frozen. The solution of **1** was thawed and added to the stirring slurry of $FeCl_2(py)_2$. The reaction mixture became a dark red solution as it warmed. The reaction was stirred at room temperature overnight. Removal of the solvent in vacuo gave an orange residue, which was extracted with Et_2O. The Et_2O solution was filtered over Celite, approximately 20 drops of THF were added, and a precipitate formed. The bright orange solid **3** was collected on a glass frit (0.445 g, 103% yield due to remaining Et_2O). Crystals suitable for X-ray diffraction were grown from a vapor diffusion of Et_2O into a THF solution of **3** at room temperature. ^{1}H NMR (500 MHz, C_6D_6): δ/ppm 151.71 (s), 77.68 (s), 71.94 (s), 30.47 (s), 15.19 (s), 9.76 (s), 4.16 (s), 1.65 (s), 1.07 (s), 0.32 (s), −6.72 (br s). UV/vis (THF) λ_{max}/nm (ε/M^{-1} cm^{-1}): 317 (16 000), 516 (1100), 560 (920, sh), 1636 (250), 1911 (180, sh). μ_{eff} (C_6D_6, 295 K): 5.1(1) μ_B. Comb. Anal. for $[C_{46}H_{47}FeN_4]^-[LiC_{16}H_{32}O_4]^+$, Calcd: C, 73.94; H, 7.91; N, 5.55. Found: C, 73.80; H, 7.81; N, 5.79.

[(tpe)Co(py)][Li(THF)$_4$] (4). In separate 20 mL scintillation vials, **1** (482 mg, 0.831 mmol) and PhLi (220 mg, 2.61 mmol) were each dissolved in 3 mL of THF and cooled in a −35 °C freezer. The cold solution of **1** was added to the PhLi solution and stirred at room temperature for 30 min. In another 20 mL vial, $CoCl_2(py)_2$ (241 mg, 0.835 mmol) was slurried in 3 mL of THF. The vials containing deprotonated **1** and $CoCl_2(py)_2$ were placed in a liquid nitrogen cooled cold well until frozen. The solution of **1** was thawed and added to the stirring slurry of $CoCl_2(py)_2$. The reaction mixture became a very dark purple-blue solution as it warmed. The reaction was stirred at room temperature for 3 h. Removal of the solvent in vacuo gave a black-blue residue, which was dissolved in benzene. The benzene solution was filtered over Celite and lyophilized. The resulting dark blue solid was dissolved in Et_2O, 10 drops THF were added, and the solution was cooled to −35 °C. A dark blue precipitate, **4**, formed and was collected on a glass frit (0.581 g, 69% yield). Crystals suitable for X-ray diffraction were grown from a vapor diffusion of hexanes into a THF solution of **4** at room temperature. ^{1}H NMR (500 MHz, CD_2Cl_2): δ/ppm 165.25 (s), 93.99 (s), 46.56 (s), 24.55 (s), 7.04 (br s), 6.51 (s), 5.97 (s), 3.86 (s), 1.55 (s), 1.17 (s), −4.38 (s). UV/vis (THF) λ_{max}/nm (ε/M^{-1} cm^{-1}): 325 (12 000), 550 (850), 621 (730), 650 (860), 998 (200), 1250 (90, sh). μ_{eff} (C_6D_6, 295 K): 4.84(5) μ_B. Comb. Anal. for $[C_{46}H_{47}CoN_4]^-[LiC_{16}H_{32}O_4]^+$, Calcd: C, 73.72; H, 7.88; N, 5.55. Found: C, 73.61; H, 7.78; N, 5.62.

[(tpe)Ni(py)][Li(THF)$_4$] (5). In separate 20 mL scintillation vials, **1** (27.9 mg, 0.0481 mmol) and PhLi (12.9 mg, 0.154 mmol) were each dissolved in 3 mL of THF and cooled in a −35 °C freezer. The cold solution of **1** was added to the PhLi solution and stirred at room temperature for 30 min. In another 20 mL vial, $NiCl_2(py)_2$ (14.4 mg, 0.0500 mmol) was slurried in 3 mL of THF with ∼0.5 mL of pyridine. The vials containing deprotonated **1** and $NiCl_2(py)_2$ were placed in a liquid nitrogen cooled cold well until frozen. The solution of **1** was thawed and added to the stirring slurry of $NiCl_2(py)_2$. The reaction mixture became a green solution as it warmed. The reaction was stirred at room temperature overnight. Removal of the solvent in vacuo gave a dark gray residue. The residue was extracted into 5 mL of benzene and filtered through a Celite plug to remove lithium chloride. Removal of the solvent in vacuo gave a gray powder (37.0 mg, 76%). Crystals suitable for X-ray diffraction were grown from a vapor diffusion of hexanes into a THF solution of **5** at room temperature. ^{1}H NMR (500 MHz, C_6D_6): δ/ppm 118.62 (br s), 109.37 (s), 43.39 (s), 27.73 (s), 13.97 (s), 6.27 (s), 5.76 (s), 3.24 (s), 1.78 (s), 1.27 (s), −1.36 (s). UV/vis (THF) λ_{max}/nm (ε/M^{-1} cm^{-1}): 319 (13 000), 398 (1500, sh), 504 (500, sh), 631 (570), 800 (120), 928 (60). μ_{eff} (C_6D_6, 295 K): 2.91(5) μ_B. Comb. Anal. for $[C_{46}H_{47}NiN_4]^-[LiC_{16}H_{32}O_4]^+$, Calcd: C, 73.73; H, 7.88; N, 5.55. Found: C, 73.67; H, 7.72; N, 5.65.

[(tpe)Zn(py)][Li(THF)$_4$] (6). In separate 20 mL scintillation vials, **1** (0.288 g, 0.497 mmol) and PhLi (130 mg, 1.54 mmol) were each dissolved in 3 mL of THF and cooled in a −35 °C freezer. The cold solution of **1** was added to the PhLi solution and stirred at room temperature for 30 min. In another 20 mL vial, $ZnCl_2$ (70 mg, 0.51 mmol) was slurried in 3 mL of THF with ∼0.5 mL of pyridine. The vials containing deprotonated **1** and $ZnCl_2$ were placed in a liquid nitrogen cooled cold well until frozen. The solution of **1** was thawed and added to the stirring slurry of $ZnCl_2$. The reaction mixture became a bright yellow solution as it warmed. The reaction was stirred at room temperature for 3 h. Removal of the solvent in vacuo gave a dark yellow residue. The residue was extracted into 5 mL of benzene and filtered through a Celite plug to remove lithium chloride and lyophilized. The resultant bright yellow powder was dissolved in Et_2O, 10 drops of THF were added, and the solution was cooled to −35 °C. A yellow precipitate, **6**, formed and was collected on a glass frit (0.234 g). The filtrate was dried in vacuo, dissolved in Et_2O, and THF was added. A second crop of **6** was collected (32 mg; total yield 266 mg, 55%). Crystals suitable for X-ray diffraction were grown from a solution of **6** in a 1:1 mixture of Et_2O and THF solution with 10 drops of TMEDA at −35 °C. ^{1}H NMR (500 MHz, C_6D_6): δ/ppm 6.70−6.68 (m, 2H, *o*-C_5H_5N), 6.61−6.58 (m, 4H, *p*-C_5H_5N, pyrrole C-*H*), 6.53 (s, 6H, -$C_6H_2(CH_3)_3$), 6.24 (br s, 3H, pyrrole C-*H*), 6.17−6.14 (m, 2H, *m*-C_5H_5N), 3.46 (m, 12H, $Li(OCH_2(CH_2)_2CH_2)_4$), 2.67 (s, 3H, $(CH_3)C(C_5H_2MesN)_3$), 2.15 (s, 18H, *o*-$C_6H_2(CH_3)_3$), 2.02 (s, 9H, *p*-$C_6H_2(CH_3)_3$), 1.35 (m, 12H, $Li(OCH_2(CH_2)_2CH_2)_4$). ^{13}C NMR (101 MHz, C_6D_6): δ/ppm 149.3, 146.9, 138.4, 137.9, 136.5, 135.3, 124.3, 106.7, 102.5, 68.4, 43.3, 26.0, 22.0, 21.3. MS (ESI$^-$) *m*/*z* $C_{46}H_{47}N_4Zn^-$ [M]$^-$, Calcd: 719.3. Found: 719.3 (observed isotope pattern matches predicted isotope pattern).

(κ^2-tpeH)Fe(py)$_2$ (7). A thawing 3 mL of THF solution of **1** (67.3 mg, 0.12 mmol) was added to solid $LiN(TMS)_2$ (38.6 mg, 0.23 mmol) and stirred for 1.5 h at room temperature, during which time the solution turned from clear pale yellow to clear magenta. This solution was frozen in a liquid nitrogen cooled cold well. $FeCl_2(py)_2$ (33.1 mg, 0.12 mmol) was slurried in 5 mL of THF and frozen. The thawing solution of deprotonated **1** was added to the thawing slurry, rinsing with room temperature THF, and was stirred for 4 h. Solvent was removed in vacuo, and the resulting residue was dissolved in Et_2O and filtered through a Celite plug. Volatiles were removed in vacuo, affording **7** (29.5 mg, 32%) as an orange-yellow powder. A sample containing 134.0 mg of **7** was analyzed by Mössbauer spectroscopy. Crystals suitable for X-ray diffraction were grown from an Et_2O solution of **7**. ^{1}H NMR (500 MHz, C_6D_6): δ/ppm 114.86, 100.30, 41.18, 34.46, 28.77, 24.87, 12.09, 9.99, 6.95, 5.20, 2.39, 1.43, −0.68, −8.40, −16.46. Comb. Anal. for $C_{51}H_{53}FeN_5$, Calcd: C, 77.36; H, 6.75; N, 8.84. Found: C, 77.24; H, 6.67; N, 8.73.

Procedure for Oxidation of [(tpe)Fe(py)][Li(THF)$_4$]. A solution of **3** (100.4 mg, 0.0997 mmol) in 5 mL of toluene was cooled to −40 °C in an acetonitrile/dry ice cooled cold well. The solution of **3** was added to cold, solid ferrocenium hexafluorophosphate (33 mg, 0.10 mmol) and stirred at −40 °C for 2 h. The solution was allowed to warm to room temperature and stirred overnight. Toluene was removed in vacuo, and approximately 2.5 mL of benzene was added. The solution was frozen and

lyophilized, then triturated in hexane and collected and dried on a glass frit. The resultant powder (74.4 mg) was analyzed by Mössbauer spectroscopy. X-ray quality crystals formed from an Et_2O solution stored at −35 °C. The major product was identified as **7** by comparison with an authentic sample as prepared above.

Procedure for Oxidation of [(tpe)Zn(py)][Li(THF)$_4$] and EPR Sample Preparation. A sample of **6** (18.7 mg, 0.0184 mmol) was dissolved in 5 mL of toluene and cooled in an acetonitrile/dry ice cooled cold well (−40 °C). The toluene solution was added to cooled solid ferrocenium hexafluorophosphate (6.1 mg, 0.018 mmol) and stirred at −40 °C for 2 h. A sample of the reaction mixture was added to a cooled EPR tube and frozen into a glass in liquid nitrogen.

VI. Computational Methods

The electronic structures of **2**−**6** were examined using *Gaussian 03*.[33] Geometry optimizations were performed using the atomic coordinates of the crystal structures as a starting point. Removal of the mesityl methyl groups resulted in collapse of the ligand structure, and thus no truncations to the ligand system were made. No symmetry was imposed upon the molecules. All optimizations were carried out unrestricted with the M05-2X[2] hybrid functional, as the B3LYP[3] functional was insufficient for estimating the ligand π-stacking effects. The 6-31G Pople basis set[15] was used for all structures, and "tight" convergence criteria were employed. In cases where the SCF failed to converge to the "tight" criteria, more reliable but more computationally expensive quadratic convergence was employed. The zinc structure was optimized as a singlet, and the remaining paramagnetic systems were optimized with multiplicities based on their magnetic moments from solution NMR determination (Evans' method:[7] Mn − sextet, Fe − quintet, Co − quartet, Ni − Triplet). Intermediate-spin calculations were also performed, but the high-spin structures were of lower energy in all cases. Single point population analyses were carried out on the optimized structures using the unrestricted B3LYP functional with "tight" convergence criteria for all complexes. The TZV(P) basis set[17] was used for transition metal atoms and the atoms within the first coordination sphere (all nitrogen), and SV(P) basis set[18] for all other main group atoms. The singlet $[(tpe)Zn(py)]^-$ structure optimization and population analysis calculations were performed using both restricted and unrestricted functionals, and the difference in energy was found to be negligible.

Spin density plots and molecular orbital pictures were generated from *Gaussian* cube files using Visual Molecular Dynamics 1.8.6.[34] and rendered using POV-Ray v3.6 for Windows.[35] Orbital parentage Mulliken population calculations, which can be found in the Supporting Information, were calculated using *QMForge*.[36]

Acknowledgment. The authors thank the American Chemical Society (PRF Grant Type G) and Harvard University for financial support. G.T.S. thanks the NSF for a predoctoral fellowship. The authors would like to thank Lee-Ping Wang and Troy Van Voorhis for insightful discussions.

Supporting Information Available: UV−vis spectra for $tpeH_3$ and $tpeLi_3$; calculated spin densities for **2**, **4**, and **5**; geometry optimized coordinates for complexes **2**−**6**; Mulliken population analyses for **2**−**6**; selected X-ray crystallographic data for **2**−**6**; full reference for ref 32. This material is available free of charge via the Internet at http://pubs.acs.org.

(33) Frisch, M. J. et al. *Gaussian 03*, revision E.01; Gaussian, Inc.: Wallingford, CT, 2004.
(34) Humphrey, W.; Dalke, A.; Schulten, K. *J. Mol. Graphics* **1996**, *14*, 33.
(35) *Persistence of Vision Raytracer*, v3.6; Persistence of Vision Pty. Ltd.: Williamstown, Victoria, Australia, 2004.
(36) Tenderholt, A. L. *QMForge*, version 2.1; Stanford University: Stanford, CA.